

Mechanically Sintered Gallium–Indium Nanoparticles

John William Boley, Edward L. White, and Rebecca K. Kramer*

Metallic nanoparticles (MNPs) have been used since ancient times.^[1] Recent advancements in science and engineering have demonstrated the utilization of MNPs for applications in a broad array of fields, including optics,^[2] medicine,^[3] memory,^[4–6] and semiconductors.^[7] Many current applications require a sintering step in order to coalesce the deposited MNPs to enable functionality; whether it be thermal,^[8,9] photonic,^[10–12] plasmonic,^[13] or chemical in nature.^[14–16] Although ambient and local temperatures of current sintering methods are significantly lower than the melting point of the bulk materials, difficulties can still arise when integrating MNPs into functional devices with other materials such as chemically or thermally sensitive polymers. Here, we introduce a new class of MNPs that are “mechanically sintered” at and below room temperature. Using eutectic gallium–indium (EGaIn) MNPs coated with Ga₂O₃ or thiol, we demonstrate particle coalescence via the application of low pressures, which ruptures the particle coatings and releases the low-viscosity liquid-metal. This phenomenon is observed morphologically through scanning electron imaging and electrically through two-probe measurements during compression. Fusing the results of this study with the unique properties of EGaIn and the semiconductive nature of Ga₂O₃^[17] will facilitate new applications across a broad array of fields such as soft robotics, conformable electronics, wireless communications, micro/nanofluidics, wearable/implantable devices, and energy storage and transport systems. We also demonstrate that EGaIn MNPs are compatible with scalable additive manufacturing technologies such as inkjet printing and can be used to fabricate flexible/stretchable integrated devices across multiple length scales.

Recent scientific progress in creating small particles of Ga–In alloy has seen potential for applications in surface-enhanced Raman spectroscopy substrates,^[18] heavy metal ion sensors,^[19,20] and photo catalysts.^[19] We focus this study on EGaIn nanoparticles (EGaInNPs) formed via sonication in ethanol, a system which has been studied,^[18] although we have achieved liquid-metal dispersions via sonication in different solvents (e.g., toluene and acetone). Two separate modalities of mechanical sintering are investigated: local/selective sintering, where local areas within a deposit of EGaIn nanoparticles (EGaInNPs) are sintered (sub-mm scale); and global sintering, where the entire deposit is sintered (at and above mm scale).

Figure 1 displays local stress-induced coalescence of EGaInNPs. The main image in Figure 1a features a deliberately

plowed pile of chips formed from a dried film of EGaInNPs (see Experimental Section). Note the occurrence of microcracks in the deposits in Figure 1, which is common in dried colloidal deposits.^[21,22] Furthermore, the stability of the chips indicates “solid-like” behavior of the deposit and high interparticle adhesion, both characteristic of the oxide coating each particle.^[23] During the plowing process, some local areas of the film experienced stresses large enough to coalesce the EGaInNPs into a continuous liquid phase (see top right detail in Figure 1a), while others experienced smaller stresses so that the film of EGaInNPs remained intact (see bottom right detail in Figure 1a). The detail views in Figure 1a highlight the drastic morphological difference between the noncoalesced and coalesced regions of the film. To confirm that particle coalescence induces electrical change, two-probe electrical measurements were taken before and after coalescence. Before coalescence, a high electrical loss through the EGaInNP network is observed, most likely from electron scattering across the interfaces and microcracks within the deposit (formed during the drying process), resulting in a high breakdown field of $\approx 50 \text{ kV m}^{-1}$ (Figure S1, Supporting Information). Note that the characteristics of this breakdown field will change to some extent depending on the

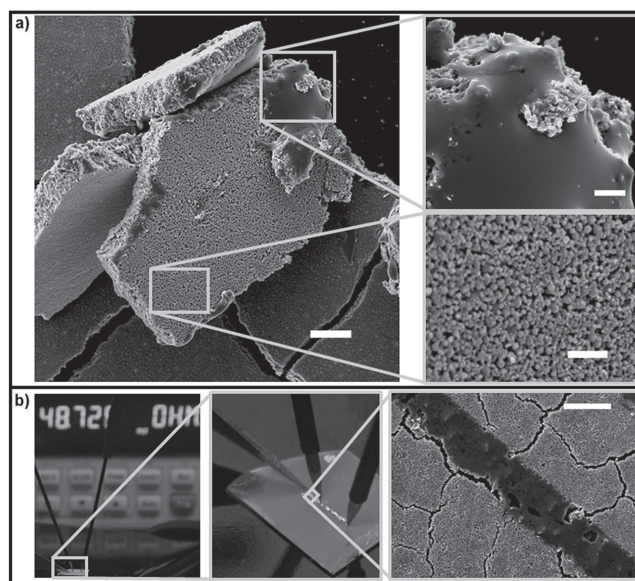


Figure 1. Observation of local mechanical sintering phenomenon. a) SEM image of plowed pile of EGaInNP chips (main) with detail views of liquid EGaIn formed during the plowing process (right-top) and intact nanoparticles (right-bottom). Scale bar in larger image is 20 μm in length. Scale bars in detail views are 5 μm in length. b) Resistance measurement ($\approx 49 \Omega$) of liquid EGaIn line (left). Detail view of drawn line (middle). Representative SEM image of drawn line revealing morphological change in area of contact from nanoparticle network to a coalesced line of liquid (right). Scale bar is 20 μm in length.

Dr. J. W. Boley, E. L. White, Prof. R. K. Kramer
School of Mechanical Engineering
Purdue University
585 Purdue Mall, West, Lafayette, IN 47907, USA
E-mail: rebeccakramer@purdue.edu



DOI: 10.1002/adma.201404790

amount of Ga_2O_3 present in the sample due to its semiconductive nature.^[17,20] However, as illustrated by Figure 1b, by selectively tapping the deposit (see Experimental Section), the coalesced area displays a low electrical resistance ($\approx 49 \Omega$) and appears as a continuous liquid film. This series of observations confirms that mechanical coalescence of EGaInNPs changes their electrical properties from nonconductive to conductive. Moreover, this process is irreversible. Once the protective layers have been ruptured and the liquid metal coalesces into a single body, its cohesion allows it to remain intact, as illustrated in Figure 1a and b. Although plowing is useful for illustrating the sintering process (as shown in Figure 1a), it is difficult to track with regard to quantifying mechanical requirements for activating the material.

Compression tests were conducted on drop-casted networks of EGaInNPs in the absence of any stabilizing agents (e.g., thiols) in order to demonstrate global sintering and to quantify the required forces to sinter particles of different sizes. The results from these experiments are summarized in Figure 2. Figure 2a shows the process for obtaining desired particle sizes (see Experimental Section). Briefly, the raw scanning electron microscope (SEM) images (Figure 2a(i)) were converted from grayscale to black and white (Figure 2a(ii)), followed by a segmentation step. The output of the segmentation step (Figure 2a(iii)) was then used to obtain the size distributions for each sample. Figure 2b shows the average particle diameter and corresponding standard deviations for different particle formation conditions. Since all samples were prepared using the same sonication conditions except for sonication time, Figure 2b

indicates that the particle size is tunable and that an increase in ultrasonic irradiation dosage results in a smaller particle size, which is in agreement with other sonication studies conducted to produce small metallic particles.^[19,24] The results from the compression tests are featured in Figure 2c (see Experimental Section for details of the experiment). In general, all samples followed the same trend: (1) an initial nonconductive state until a critical activation force is reached, followed by (2) a jump in voltage corresponding to a metal-like resistance, then (3) a dwell period, where the voltage remains relatively constant until a critical deactivation force is reached, and finally (4) a sudden drop in voltage, indicating the squeezing of the liquid metal film from beneath the punch to the surrounding environment. The first stage (a nonconductive state up to activation force) is expected considering the electrical results of the unperturbed network (Figure S1, Supporting Information). In order to gain a better understanding of the dependence of activation force on particle size, the results were recast in terms of estimated activation force per particle, as shown in Figure 2d. The activation force per particle f is the force that each particle in contact with the punch experiences at activation and was calculated by

$$f = \frac{d^2}{pD^2} F \quad (1)$$

where F is the measured activation force applied by the punch onto the sample, $D = 4.5 \pm 0.3 \text{ mm}$ is the diameter of the circular polystyrene punch, d is the average particle diameter, and p is the areal packing factor of the particles (assumed to be constant at 0.82, corresponding to a random packing arrangement).^[25] An adjusted R^2 value of 0.98 indicates that the activation force per particle increases linearly with average particle size, which agrees with a previous study on the bursting strength of microscale oil-filled particles with formaldehyde walls.^[26] The physical mechanism behind this effect comes from the naturally formed Ga_2O_3 layer surrounding each of the particles in the network. When a given particle undergoes enough strain, this viscoelastic shell will fracture, inducing an outward flow of encased EGaIn. Since this happens over all particles in contact with the punch, the liquid EGaIn released then coalesces to form pathways for metal-like electron transport.

The linear trend displayed in Figure 2d can be modeled using the theory of thin, elastic-perfectly plastic, fluid-filled membranes. Previous studies have reported that the naturally forming Ga_2O_3 outer layer of Ga–In alloys in air is inherently conformal and fast-forming.^[23,27,28] More specifically, X-ray reflectivity measurements show that the thickness of the Ga_2O_3 layer is $t \approx 0.5 \text{ nm}$, which is much smaller than the particle radii in this study.^[28] Additionally, from previous experiments, the stress–strain relationship of the Ga_2O_3 layer was found to behave elastically up to the fracture strain, after which there is no significant change in stress.^[23] Therefore, the theory of thin, elastic-perfectly plastic, fluid-filled shells is applicable. Using data from Dickey et al.'s previous report, the modulus of elasticity (E) and the yield stress (σ_y) of Ga_2O_3 are estimated to be ≈ 39 and $\approx 1 \text{ GPa}$, respectively.^[23] Interpreting the activation force as the yielding force, the results depicted in Figure 2d for the compressed network can be effectively modeled as a single incompressible fluid-filled spherical shell of the same diameter

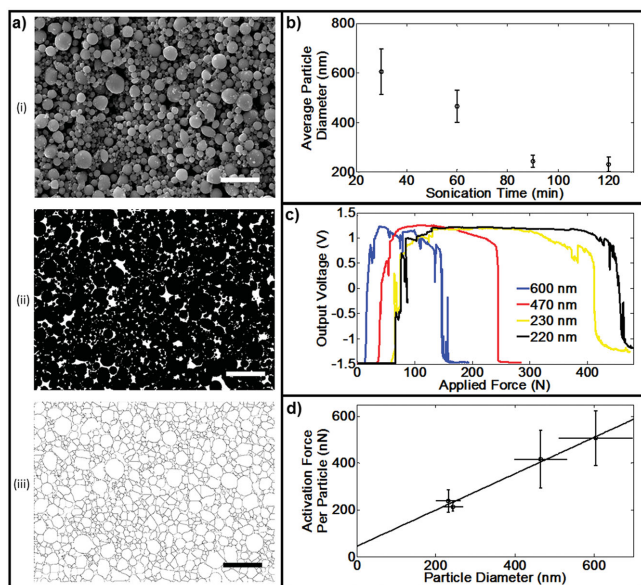


Figure 2. Characterization of EGaInNPs without stabilizing agents. a) Process map for determining particle sizes including i) the raw SEM image, ii) the black and white converted image, and iii) the resulting segmented image. Scale bars are $2 \mu\text{m}$ in length. b) Resulting average particle diameters as a function of sonication time. Uncertainty bars are two standard deviations in length. c) Representative voltage output versus applied force results from compression experiments on samples of different particle sizes. d) Estimated activation force per particle versus particle diameter. Vertical and horizontal error bars are two standard deviations in length. Line represents linear fit through the data.

squeezed between two flat plates, yielding at high deformations.^[29] Next, using the slope of the linear fit from Figure 2d ($m = 0.78 \pm 0.27 \text{ nN nm}^{-1}$) enables us to calculate the Mercadé-Prieto fitting parameter (k_e):^[29]

$$k_e = \frac{2m}{t\sigma_y} \approx 3.11 \quad (2)$$

Using this value for k_e and interpolating from Table 1 of Mercadé-Prieto's finite element results^[29] corresponds to an effective compression of 0.44*d*, which indicates that the effective particle will rupture when compressed by 44% of its original diameter. This amount of compression may be larger than that of a single particle in compression due to the effects of compaction, interparticle interactions, and the occurrence of microcracks within the deposit. The difference in the dwell period (stage three of the sintering process) stems from the amount of Ga₂O₃ present with each sample. Samples with smaller particle sizes inherently contain larger amounts of Ga₂O₃ (i.e., smaller particles result in a larger amount of surface area exposed to oxygen, resulting in increased amounts of Ga₂O₃). As the concentration of Ga₂O₃ increases, so does the mechanical rigidity, since Ga₂O₃ is known to be a viscoelastic material.^[23,28] As mechanical rigidity increases, so does its resistance to flow or deformations for a given force (i.e., effective surface tension), which explains the observed increased dwell period with decreased particle size. Figure 2c also shows an apparent gradual voltage drop throughout the dwell period. This observed drop is attributed to the gradual removal of material between the electrodes during the compression process. Moreover, the decrease in slope of this drop with decreased particle size can be explained by the increased structural stability coming from the higher amounts of oxide. The maximum output voltage achieved after reaching the activation force remained constant throughout all trials (95% confidence interval of $1.23 \pm 0.19 \text{ V}$), indicating indistinguishable electrical resistance effects from increased amounts of Ga₂O₃ with decreased particle size over the range of particle sizes tested. With the role of the Ga₂O₃ layer established in the mechanical sintering process, we now turn our focus to the effects of replacing this layer with a different material.

Steric stabilization and size reduction of MNPs with thiols is well documented.^[18,30] However, it is also important to understand the effects of thiols on the morphology and sintering performance of the deposited material. Therefore, we developed a process to arrive at an appropriate thiol concentration for a given sonication condition that leverages the steric stabilization of the thiol while preserving the mechanical sintering property. **Figure 3** summarizes the results obtained by experiments conducted to characterize these effects for a fixed sonication condition (see Experimental Section). Beginning with deposit morphology (see Figure 3a), for thiol concentrations $\leq 1 \times 10^{-3} \text{ M}$ it is evident that the particles are polydispersed. However, as we increase the thiol concentration between 0 and $0.5 \times 10^{-3} \text{ M}$, we observe a more bimodal-like distribution with increased clustering of similarly sized particles. We attribute this effect to insufficient thiol levels, where non-thiol-capped particles are likely to aggregate since there is no thiol providing steric stabilization. This trend levels off at a concentration of $1 \times 10^{-3} \text{ M}$,

where the particles seem to be mostly monodispersed. The average particle diameter of the EGaInNPs for the $1 \times 10^{-3} \text{ M}$ samples ($180 \pm 32 \text{ nm}$) is considerably smaller than that of samples without thiol ($465 \pm 65 \text{ nm}$); this effect of decreased particle size with increased thiol concentration is consistent with the observations of Hohman et al.^[18] Increasing thiol concentration beyond $1 \times 10^{-3} \text{ M}$ results in agglomerations of the EGaInNPs, which appears to be a result of excess thiols. The excess thiols appear on the samples as a continuous clear film surrounding the EGaInNP aggregates (see the detail image of the $5 \times 10^{-3} \text{ M}$ sample in Figure 3a). Rinsing the higher thiol concentration samples ($\geq 3 \times 10^{-3} \text{ M}$) prior to deposition verifies the presence of this film (see the Supporting Information). Therefore, the optimized ratio of EGaIn to thiol concentration for this system is $\approx 400:1$ by weight.

Compression tests were also conducted to see how thiols affect the mechanical sintering phenomenon. As evident in Figure 3, the required activation force (F) applied by the punch remains consistent for thiol concentrations $\leq 1 \times 10^{-3} \text{ M}$. However, the significant size reduction associated with the $1 \times 10^{-3} \text{ M}$ concentration samples results in a much lower activation force per particle ($f \approx 25 \text{ nN}$). This value is significantly less than that predicted by the linear model for thiol-free EGaInNPs of the same size shown in Figure 2d (168 nN). This observed reduction in activation force per particle indicates a combined effect of softening, weakening, or thinning of the EGaInNP surface in the presence of the thiols. The rupture mechanism facilitating the coalescence of the thiol-capped EGaInNPs is considered to be the same as that of the oxide-encased particles. These results suggest that the thiol coating ruptures more easily than the Ga₂O₃ coating, and therefore the effective surface tension of the thiol-capped particles must be lower than that of the Ga₂O₃ coated particles. This decrease in effective surface tension facilitates the production of smaller particles in the presence of thiol, which also agrees with explanations given by Hohman et al.^[18] In this regard, we expect size reduction in the presence of thiol to occur across multiple sonication conditions. Furthermore, as indicated by Figure 3b,c, the presence of excess thiol inhibits the formation of percolation pathways for the EGaIn during compression, resulting in increased activation forces and film resistances, as well as their corresponding uncertainties.

Additional experiments were conducted to produce smaller features by selective mechanical sintering. As shown in **Figure 4**, arrays of smaller lines can be formed simply by scaling down the sintering tool. In this study, $1 \mu\text{m}$ coalesced EGaIn lines were formed, which are half the size of previously reported features.^[31] Reducing the sintering tool size even further may achieve submicrometer features.

Mechanically sinterable EGaInNP dispersions also provide a means for inkjet printing of EGaIn devices, a process not applicable to the bulk material in an oxygen-containing environment.^[32] However, by dispersing EGaInNPs, the resulting material displays properties more closely resembling the inkjettable carrier solvent. As shown in **Figure 5**, this material can be inkjet printed directly onto an elastomer glove surface to form arrays of strain gauges with intricate wiring and contact pads. This result represents an opportunity to manufacture liquid-metal devices using high-yield, high-throughput, and scalable processes.

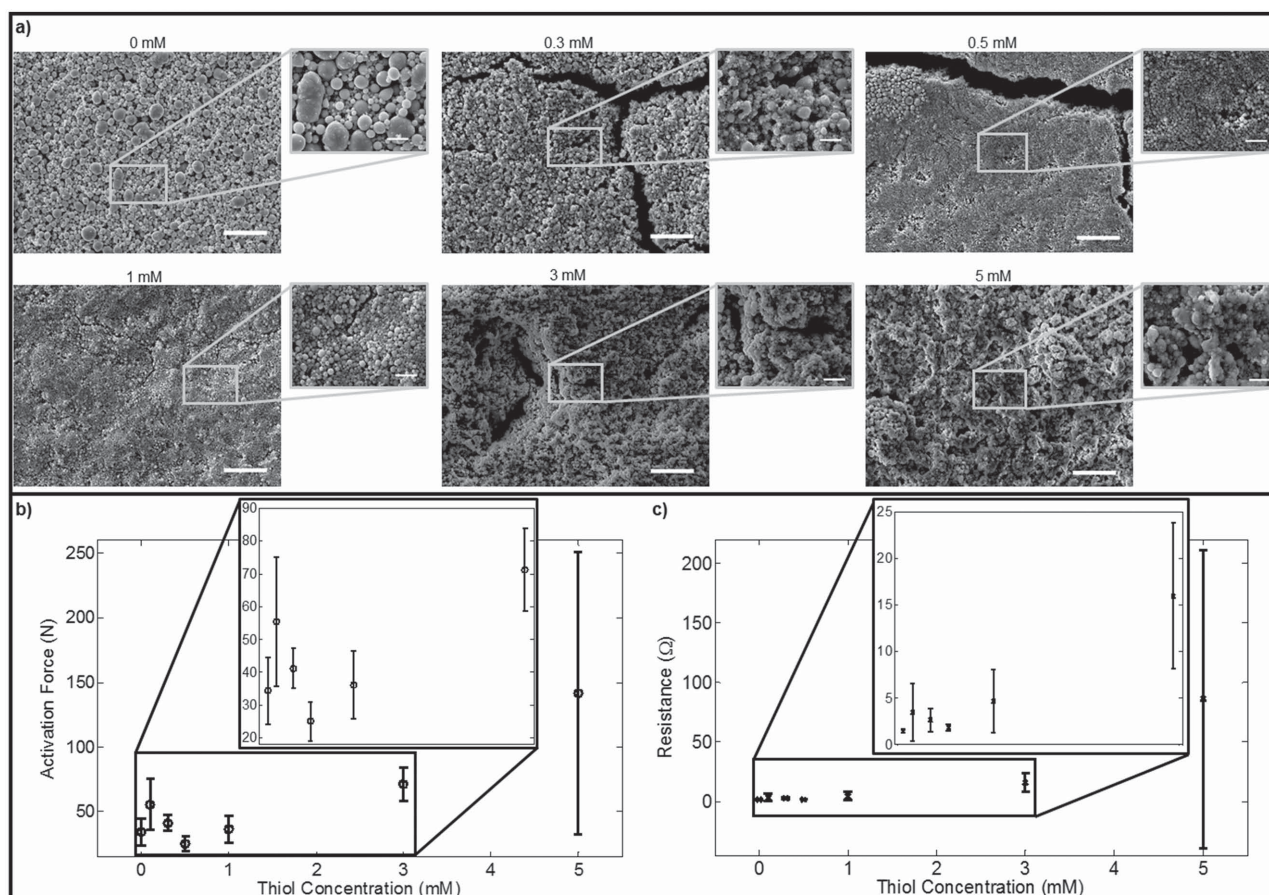


Figure 3. Effects of thiol concentration. a) Representative SEM images of deposited samples prepared with different concentrations of thiol. Scale bars of main images are 10 μm in length. Scale bars of corresponding detail images are 2 μm in length. b) Thiol dependence of activation force for all concentrations considered, with accompanying detail at lower concentrations. Error bars are two standard deviations in length. c) Thiol dependence of resulting resistance across coalesced sample after activation. Inset shows details of dependence at lower concentrations. Error bars are two standard deviations in length.

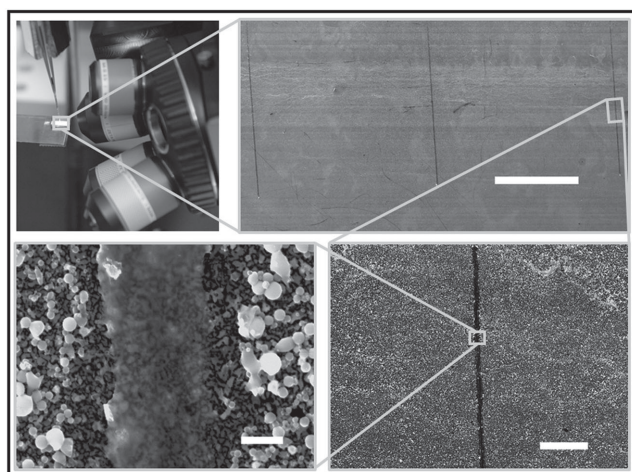


Figure 4. Small scale line coalescence. Setup used to write arrays of $\approx 1 \mu\text{m}$ wide coalesced lines (top-left); detail view of an array of written lines (top-right), scale bar is 500 μm in length; detail view featuring a single coalesced line (bottom-right), scale bar is 20 μm in length; and detail view of single coalesced line revealing liquid-phase morphology (bottom-left), scale bar is 500 nm in length.

To summarize, we have employed sonication and thiol self-assembly to create EGaInNPs with tunable average particle sizes from $\approx 600 \text{ nm}$ down to $\approx 180 \text{ nm}$. We have characterized this material as a new class of mechanically sintered MNPs. The EGaInNPs encased with Ga_2O_3 requires an activation force per particle that scales with average particle size (sensitivity of $\approx 0.78 \text{ nN nm}^{-1}$), while capping EGaInNPs with thiol displays a softening effect ($\approx 15\%$ smaller activation force per particle). In this study, we also demonstrate two modes of mechanical sintering: global sintering, with the ability to sinter entire deposits at or above the mm scale; and local/selective sintering, with the ability to sinter areas within deposits as small as 1 μm and potentially smaller. Finally, we also show applicability to inkjet printed devices, a process not applicable to bulk EGaIn in an oxygen-containing environment. Future work may include dynamic compression/rupture studies evaluating both individual particles and the complex interactions in particle films. Other future investigations will include the application of this process to create stretchable conductors, sensors, mechanical switches and integrated liquid circuits, with applications in sensory skins, stretchable electronics, and active conformable devices.

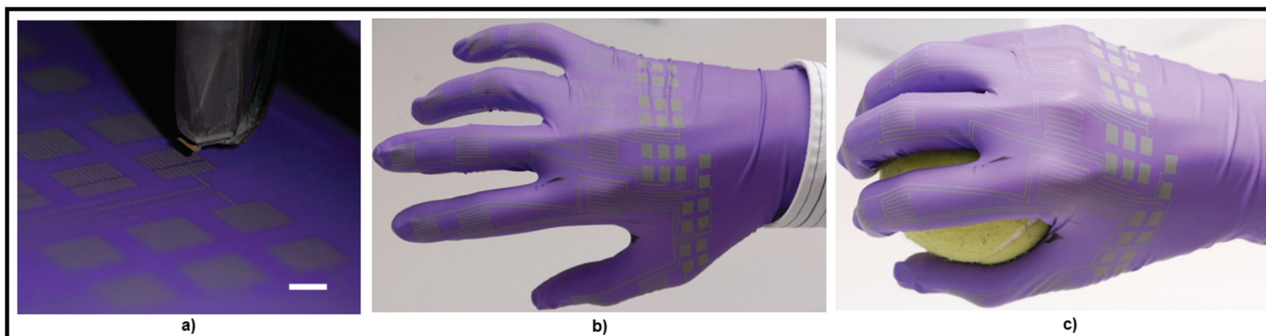


Figure 5. Inkjet printing of EGaInNPs. a) Photograph of inkjet system printing EGaInNP dispersion. Scale bar is 5 mm in length. b) Human hand wearing inkjet functionalized nitrile glove with arrays of strain gauges, intricate wiring, and contact pads comprised of EGaInNPs. c) Same hand holding a tennis ball, demonstrating stretchability of the electronics.

Experimental Section

Preparation of EGaInNPs: All EGaInNP samples were made using a QSonica Q700 microtip sonicator (part number 4417) at 30% amplitude (96 μm) inserted a fixed distance (≈ 1 mm) above the bottom of a Kimble Chase 3 dram glass vial (See Figure S2a, Supporting Information). All samples including thiol were sonicated for 60 min. Prior to sonication, all samples were filled with a fixed mass (362 mg) of EGaIn (product number 495425 as purchased from Sigma Aldrich) using a syringe and a mass balance (OHAUS PioneerTM). Following this, 4 mL ethanol/thiol solutions were added to the vial by micropipetting (BioPette Plus BPP1000) a prescribed volume combination of highly concentrated ethanol/thiol solution and neat ethanol (Koptec part number V1001) to achieve the desired concentration. High concentration thiol solutions were made by adding a measured amount of thiol (3-Mercapto-*N*-nonylpropionamid; part number 686492 as purchased from Sigma Aldrich) mass to a glass vial, followed by the addition of the appropriate volume of ethanol. The resulting mixture was shaken vigorously followed by a 1 min bath sonication (Branson 1800) at room temperature to achieve uniformity. Each EGaInNP dispersion sample was allowed to settle for 24 h. Just prior to creating samples for particle characterization and compression testing, each sample was shaken vigorously and magnetically stirred for 5 min to ensure uniform dispersion of EGaInNP. Uniformity of EGaInNP concentration was confirmed by measuring the post-evaporation mass of 1 mL samples. Multiple dispersions ($N = 5$) were made for each set of conditions (thiol concentration and sonication time) for confidence. High speed centrifugation was employed to rinse the 3 and 5×10^{-3} M samples to confirm the presence of excess thiols. Sonicated samples were subjected to 6238 relative centrifugal force in a centrifuge (Cole Parmer WU-39065-05) for 20 min. After centrifugation, the aliquot was discarded, fresh ethanol was added, and the pellet was resuspended in a light sonication bath (Branson 1800) for ≈ 3 min. This process was repeated twice for each sample.

Plowing and Line Drawing: The plowed pile of EGaInNP chips shown in Figure 1a was formed by drop casting 50 μL of EGaInNP dispersion onto a Si wafer (0.0035–0.0038 Ωcm Si wafers (Silicon Sense, Inc.)), followed by a line-carving step with a diamond scribe. The coalesced line of liquid EGaIn was formed by gently tapping a similarly drop-casted film of EGaInNPs with an X-Acto knife.

***I*-*V* Characterization:** Samples for *I*-*V* characterization were made by spin-coating EGaInNPs/ethanol dispersions (0×10^{-3} M) onto Kapton substrates. Two-probe measurements were conducted on the non-sintered samples by positioning electrical probes (Signatone SE-TZ) via micromanipulators (Signatone S-926) onto the sample a spacing of ≈ 1 mm apart tracking the supplied voltage and measured current through a Keithley 2410-C SourceMeter. Voltage sweeps were performed manually (See Figure S1, Supporting Information), waiting ≈ 30 s for signal stabilization after each step prior to recording.

Particle Characterization: Samples for particle characterization were prepared by depositing 50 μL via micropipette (BioPette Plus BPP200) onto Si wafers (Silicon Sense, Inc., 0.0035–0.0038 Ωcm) (See bottom-middle image of Figure S2b, Supporting Information for process). Scanning electron microscope (SEM) images were then obtained (Philips XL-40 FEI, 15 kV, 3 μm beam spot size). All images were analyzed using the following procedure through ImageJ: (1) each raw grayscale SEM image was converted to a binary image (Image \rightarrow Adjust \rightarrow Threshold, with a lower cutoff of ≈ 15 and an upper cutoff of ≈ 230 and Dark background option); (2) each resulting binary image was segmented using the built-in ImageJ watershed routine (Process \rightarrow Binary \rightarrow Watershed); (3) the sizes for all segmented particles were obtained using ImageJ's particle analysis package (Analyze \rightarrow Analyze Particles, with size range going from 10 square pixel units to infinity, circularity from 0 to 1, showing bare outline of particles); (4) the diameter for each particle was computed from the area output by ImageJ under a spherical approximation. This process was repeated over multiple experimental trials ($N = 5$) for each formulation condition. Energy-dispersive X-ray spectroscopy (EDS) was employed (FEI Quanta 3D FEG Dual-beam SEM with an Oxford INCA Xstream-2 silicon drift detector with Xmax 80 window) to measure elemental composition in samples (results shown in Figures S3–S7, Supporting Information). The SEM system used to inspect the morphology of the rinsed samples (results shown in Figures S8 and S9, Supporting Information) is the same used for particle characterization on the thiol free and nonrinsed samples.

Compression Experiments: Polydimethylsiloxane (PDMS) devices containing copper wires were made to serve as EGaInNP reservoirs for the compression tests (see Figure S2b, Supporting Information, far right detail image for photograph of device). Specifically, PDMS (Sylgard 184) was mixed as received from Dow Corning with a 10:1 weight ratio of base to crosslinking agent. The resulting mixture was spincoated onto glass slides, yielding a thickness of ≈ 350 μm . After fixing copper wires to the cured PDMS films, a second coat of ≈ 200 μm was applied via spincoating. Finally, samples were cut and circular reservoirs ≈ 200 μm deep with a diameter of ≈ 2.5 mm were made in a single step using a laser ablation technique. The compression tests were conducted using a materials tester. Each device was fixed to a platen loaded into a single column materials testing unit (Instron model 3345) fitted with a 1 kN load cell. The electrodes of the device were attached to a Wheatstone bridge, where the three other legs of the bridge were 20 Ω resistors and the voltage supply was 3 V. The output voltage of the bridge was connected to the data acquisition of the materials tester and tracked with applied force during the experiments. All samples were compressed at a rate of 1 mm min^{-1} . This process was repeated over multiple experimental trials ($N = 5$) for each formulation condition.

Small Scale Line Drawing Experiments: Arrays of thin lines were produced (See Figure 4 for photograph of setup) via mechanical sintering by moving an EGaInNP-deposited sample (1×10^{-3} M) in

straight lines relative to a stationary mechanically cleaved Si needle (radius of needle $\approx 1 \mu\text{m}$). The substrate motion relative to the needle was controlled through a three-axis motion system (PI: 2 X M-531.DD, M-501.PD, C-843.41). Prior to motion, contact between the Si needle and the sample was observed through a 3D optical profiler (Zeta-20 with a customized tiltable turret).

Inkjet Printing Experiments: The ink used in the inkjet experiments were $0.5 \times 10^{-3} \text{ M}$ thiol samples sonicated at 60 min and filtered through a $1 \mu\text{m}$ polytetrafluoroethylene syringe filter (Cole-Parmer 32816-34). Substrates employed for these experiments were purple nitrile gloves (Kimberly-Clark) precleaned with ethanol. All inkjet printing experiments were conducted using a single $\approx 65 \mu\text{m}$ orifice nozzle from an HP thermal inkjet picojet system. Samples were manipulated via two-axis stage (Anorad-XKY-C-150-150-AAA0 stage controlled by Anorad-CM-2 controller). Printing commands were employed through in-house software.

Supporting Information

Supporting Information is available from the Wiley Online Library or from the author.

Acknowledgements

We would like to thank Professor Dimitrios Peroulis and Dr. Nithin Raghunathan for access to and training on electrical characterization equipment. Many thanks to Professor George T.-C. Chiu for access to the inkjet system employed in this study and to the HP Corvallis team for providing the inkjet print-head system. We would also like to thank Michelle Yuen for help with ImageJ and photography and Jennifer Case for finding literature. Special thanks to Alex Bottiglio for cover art work. Additional thanks to Chia-Ping Huang of the Purdue Life Science Microscopy Facility and to Dr. Seok-Hee Hyun for technical support on the high resolution EDS system. E.L.W. is supported by the National Science Foundation Graduate Research Fellowship Program under Grant No. DGE-1333468. Any opinions, findings, and conclusions or recommendations expressed in this material are those of the authors and do not necessarily reflect the views of the National Science Foundation.

Received: October 16, 2014

Revised: December 22, 2014

Published online: February 27, 2015

- [1] M.-C. Daniel, D. Astruc, *Chem. Rev.* **2004**, *104*, 293.
 [2] C. J. Murphy, T. K. Sau, A. M. Gole, C. J. Orendorff, J. Gao, L. Gou, S. E. Hunyadi, T. Li, *J. Phys. Chem. B* **2005**, *109*, 13857.
 [3] L. Zhang, F. X. Gu, J. M. Chan, A. Z. Wang, R. S. Langer, O. C. Farokhzad, *Clin. Pharmacol. Ther.* **2008**, *83*, 761.
 [4] S. Paul, C. Pearson, A. Molloy, M. A. Cousins, M. Green, S. Kolliopoulou, P. Dimitrakakis, P. Normand, D. Tsoukalas, M. C. Petty, *Nano Lett.* **2003**, *3*, 533.
 [5] K. Szot, W. Speier, G. Bihlmayer, R. Waser, *Nat. Mater.* **2006**, *5*, 312.
 [6] W. Guan, S. Long, M. Liu, Z. Li, Y. Hu, Q. Liu, *J. Phys. D: Appl. Phys.* **2007**, *40*, 2754.
 [7] J. Park, J. Joo, S. Kwon, Y. Jang, T. Hyeon, *Angew. Chem. Int. Ed.* **2007**, *46*, 4630.
 [8] K.-S. Moon, H. Dong, R. Maric, S. Pothukuchi, A. Hunt, Y. Li, C. P. Wong, *J. Electron. Mater.* **2005**, *34*, 168.
 [9] T. Bhuvana, W. Boley, B. Radha, B. D. Dolash, G. Chiu, D. Bergstrom, R. Reifengerger, T. S. Fisher, G. U. Kulkarni, *Micro Nano Lett.* **2010**, *5*, 296.
 [10] J. Perelaer, M. Klokkenburg, C. E. Hendriks, U. S. Schubert, *Adv. Mater.* **2009**, *21*, 4830.
 [11] D. Angmo, T. T. Larsen-Olsen, M. Jørgensen, R. R. Søndergaard, F. C. Krebs, *Adv. Energy Mater.* **2013**, *3*, 172.
 [12] J. Chung, S. Ko, N. R. Bieri, C. P. Grigoropoulos, D. Poulidakos, *Appl. Phys. Lett.* **2004**, *84*, 801.
 [13] I. Reinhold, C. E. Hendriks, R. Eckardt, J. M. Kranenburg, J. Perelaer, R. R. Baumann, U. S. Schubert, *J. Mater. Chem.* **2009**, *19*, 3384.
 [14] S. Magdassi, M. Grouchko, O. Berezin, A. Kamyshny, *ACS Nano* **2010**, *4*, 1943.
 [15] M. Grouchko, A. Kamyshny, C. F. Mihailescu, D. F. Anghel, S. Magdassi, *ACS Nano* **2011**, *5*, 3354.
 [16] S. B. Walker, J. A. Lewis, *J. Am. Chem. Soc.* **2012**, *134*, 1419.
 [17] M. Higashiwaki, K. Sasaki, A. Kuramata, T. Masui, S. Yamakoshi, *Appl. Phys. Lett.* **2012**, *100*, 013504.
 [18] J. N. Hohman, M. Kim, G. A. Wadsworth, H. R. Bednar, J. Jiang, M. A. LeThai, P. S. Weiss, *Nano Lett.* **2011**, *11*, 5104.
 [19] W. Zhang, J. Z. Ou, S.-Y. Tang, V. Sivan, D. D. Yao, K. Latham, K. Khoshmanesh, A. Mitchell, A. P. O'Mullane, K. Kalantar-zadeh, *Adv. Funct. Mater.* **2014**, *24*, 3799.
 [20] V. Sivan, S.-Y. Tang, A. P. O'Mullane, P. Petersen, N. Eshtiahi, K. Kalantar-zadeh, A. Mitchell, *Adv. Funct. Mater.* **2013**, *23*, 137.
 [21] J. Ma, G. Jing, *Phys. Rev. E* **2012**, *86*, 061406.
 [22] A. G. Mailer, P. S. Clegg, *J. Colloid Interface Sci.* **2014**, *417*, 317.
 [23] M. D. Dickey, R. C. Chiechi, R. J. Larsen, E. A. Weiss, D. A. Weitz, G. M. Whitesides, *Adv. Funct. Mater.* **2008**, *18*, 1097.
 [24] K. S. Suslick, *Science* **1990**, *247*, 1439.
 [25] H. H. Kausch, D. G. Fesko, N. W. Tschoegl, *J. Colloid Interface Sci.* **1971**, *37*, 603.
 [26] Z. Zhang, R. Saunders, C. R. Thomas, *J. Microencapsulation* **1999**, *16*, 117.
 [27] R. C. Chiechi, E. A. Weiss, M. D. Dickey, G. M. Whitesides, *Angew. Chem. Int. Ed.* **2008**, *47*, 142.
 [28] M. J. Regan, H. Tostmann, P. S. Pershan, O. M. Magnussen, E. DiMasi, B. M. Ocko, M. Deutsch, *Phys. Rev. B* **1997**, *55*, 10786.
 [29] R. Mercadé-Prieto, R. Allen, D. York, J. A. Preece, T. E. Goodwin, Z. Zhang, *Chem. Eng. Sci.* **2011**, *66*, 1835.
 [30] R. A. Caruso, M. Ashokkumar, F. Grieser, *Langmuir* **2002**, *18*, 7831.
 [31] B. A. Gozen, A. Tabatabai, O. B. Ozdoganlar, C. Majidi, *Adv. Mater.* **2014**, *26*, 5211.
 [32] J. W. Boley, E. L. White, G. T.-C. Chiu, R. K. Kramer, *Adv. Funct. Mater.* **2014**, *24*, 3474.